28. T. Dalsgaard, F. Bak, *Appl. Environ. Microbiol.* **60**, 291 (1994).
29. R. G. L. McCready, W. D. Gould, F. D. Cook, *Arch. Microbiol.* **135**, 182 (1983).
30. A. C. Redfield, B. H. Ketchum, F. A. Richards, in *The Sea*, N. M. Hill, Ed. (Academic Press, London, 1963), vol. 2, pp. 26–77.
31. M. M. Jensen, J. Petersen, T. Dalsgaard, B. Thamdrup, *Mar. Chem.* **113**, 102 (2009).
32. G. Lavik *et al.*, *Nature* **457**, 581 (2009).

33. We thank the captain and crew of the *Agor Vidal Gormaz* from the Chilean Navy for their kind support, and the Agouron Institute, the Danish National Research Foundation, the Gordon and Betty Moore Foundation, and the Chilean Fondap Program for financial support. Additional thanks to G. Alarcón, G. Friederich, and J. Jennings for operational and experimental support. The genome sequence data are accessible on NCBI's Sequence Read Archive via accession number SRA025088.

Supporting Online Material
www.sciencemag.org/cgi/content/full/science.1196889/DC1
Materials and Methods
Figs. S1 to S8
Tables S1 to S4
References

24 August 2010; accepted 28 October 2010
Published online 11 November 2010;
10.1126/science.1196889

Dynamical Response of the Tropical Pacific Ocean to Solar Forcing During the Early Holocene

Thomas M. Marchitto,[1]* Raimund Muscheler,[2] Joseph D. Ortiz,[3] Jose D. Carriquiry,[4] Alexander van Geen[5]

We present a high-resolution magnesium/calcium proxy record of Holocene sea surface temperature (SST) from off the west coast of Baja California Sur, Mexico, a region where interannual SST variability is dominated today by the influence of the El Niño–Southern Oscillation (ENSO). Temperatures were lowest during the early to middle Holocene, consistent with documented eastern equatorial Pacific cooling and numerical model simulations of orbital forcing into a La Niña–like state at that time. The early Holocene SSTs were also characterized by millennial-scale fluctuations that correlate with cosmogenic nuclide proxies of solar variability, with inferred solar minima corresponding to El Niño–like (warm) conditions, in apparent agreement with the theoretical "ocean dynamical thermostat" response of ENSO to exogenous radiative forcing.

The influence of solar variability on Earth's climate over centennial to millennial time scales is the subject of considerable debate. The change in total solar irradiance over recent 11-year sunspot cycles amounts to <0.1%, but greater changes at ultraviolet wavelengths (*1*) may have substantial impacts on stratospheric ozone concentrations, thereby altering both stratospheric and tropospheric circulation patterns (*2*). Estimates of the secular increase in total irradiance since the late 17th century Maunder sunspot minimum range from ~0.05 to 0.5% (*1*). Values in the middle of this range are sufficient to force the intermediate-complexity Zebiak-Cane model of El Niño–Southern Oscillation (ENSO) dynamics into a more El Niño–like state during the Little Ice Age (A.D. ~1400 to 1850) (*3*), a response dubbed the "ocean dynamical thermostat" because negative (or positive) radiative forcing results in dynamical ocean warming (or cooling, respectively) of the eastern tropical Pacific (ETP) (*4*). This model prediction is supported by paleoclimatic proxy reconstructions over the past millennium (*3*, *5*, *6*). In contrast, fully coupled general circulation models (GCMs) lack a robust thermostat response because of an opposing tendency for the atmospheric circulation itself to strengthen under reduced radiative forcing (*7*).

ENSO is a leading source of interannual climate variability over large regions of the globe, so it is crucial to gain an improved understanding of its past responses to external forcing at various time scales. Tropical fossil corals provide the most reliable means for reconstructing ENSO conditions from the past (*5*), but the record is currently too fragmented to test for any relation to persistent solar forcing before the past millennium. Few sea surface temperature (SST) reconstructions from well-placed tropical Pacific sediment cores have sufficient temporal resolution to address this question.

Sediment core composite MV99-GC41/PC14 was raised from a water depth of 540 m on the floor of Soledad Basin, which is located off the west coast of Baja California Sur, Mexico (25.2°N, 112.7°W), and has an effective sill depth of 290 m (*8*). Although this site is just outside of the tropical band, modern conditions here are strongly teleconnected to ENSO. The modern annual cycle of SST has an amplitude of ~8°C on average, with minimum temperatures during spring, the season of strongest coastal upwelling (*9*, *10*). Yet interannual variability in SST is much more strongly dependent on ENSO than on local upwelling winds. Over the 30-year period covered by satellite observations, the Niño 3 index explains 37% of the monthly SST anomaly near Soledad Basin (correlation coefficient $r = 0.61$ maximum correlation with a 2-month lag), whereas the local upwelling index explains only 2% ($r = -0.16$ with zero lag) (Fig. 1). ENSO is crucial for SST because the regional thermocline deepens during El Niño years, so that even with vigorous local upwelling the ascending waters are warmer than during La Niña or neutral years (*11*). Recent spring SST minima have ranged from 17°C during strong La Niñas to 20°C during

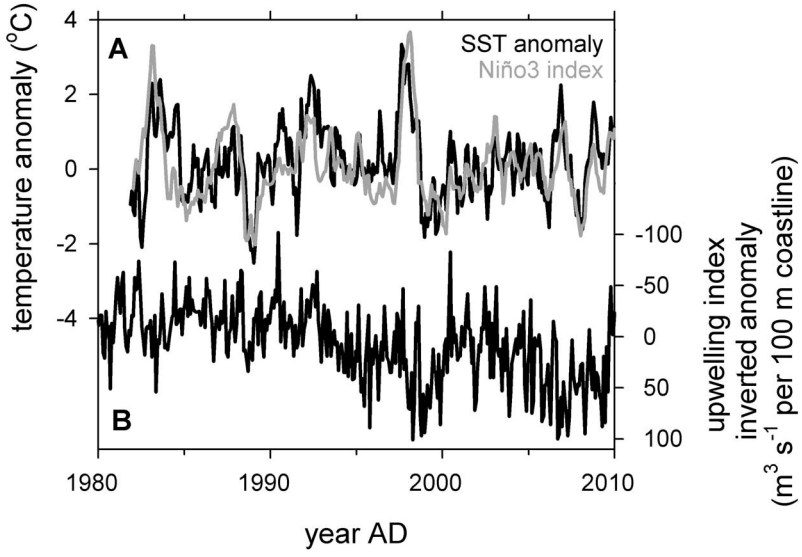

Fig. 1. (**A**) Monthly SST anomaly for the 1° grid cell situated over Soledad Basin (black) (*9*), compared to the monthly Niño 3 SST index on the same vertical scale but lagged by 2 months (gray) (*9*) and (**B**) the local (24°N, 113°W) monthly upwelling index (offshore Ekman transport computed from wind stress) anomaly (*10*), shown inverted.

[1]Department of Geological Sciences and Institute of Arctic and Alpine Research, University of Colorado, Boulder, CO 80309, USA. [2]Department of Earth and Ecosystem Sciences, Lund University, S-223 62 Lund, Sweden. [3]Department of Geology, Kent State University, Kent, OH 44242, USA. [4]Department of Environmental Geosciences, Universidad Autónoma de Baja California, Ensenada, Baja California 22830, Mexico. [5]Lamont-Doherty Earth Observatory, Columbia University, Palisades, NY 10964, USA.

*To whom correspondence should be addressed. E-mail: tom.marchitto@colorado.edu

El Niños. Surface warming off the coast of Baja California Sur can be further enhanced under El Niño conditions by the northeastward expansion of subtropical surface waters that effectively block the admixture of southward-flowing subarctic (California Current) waters (*12*).

An age model based on 22 calibrated accelerator mass spectrometry radiocarbon dates (fig. S1) reveals that the composite core spans the past 13.9 thousand years (ky) with an average sedimentation rate of >1 m ky^{-1}. During the Holocene, the sediments are laminated, indicating negligible bioturbation under low-O_2 conditions on the sea floor (*8*). Preservation of planktonic foraminifera is excellent throughout the core, with glassy tests and spines commonly present. We measured the SST proxy Mg/Ca in the planktonic foraminifer *Globigerina bulloides* (*13*), which lives at the sea surface primarily during the spring peak upwelling season along this margin (*14*). Samples were nominally spaced at 5-cm intervals and contained 30 to 60 foraminifera each, so each measurement theoretically averages 30 to 60 month-long (foraminiferal lifespan) upwelling-season snapshots spread over roughly a decade (1-cm sample width), with ~50-year spacing between samples. Although not capable of resolving the typical ENSO periodicities of 2 to 7 years, this sampling is sufficient to detect any multicentennial/millennial-scale changes in spring SSTs.

Our Mg/Ca-based SST reconstruction indicates that early to middle Holocene [~4 to 10 thousand years ago (ka)] spring temperatures were ~1°C cooler, on average, than during the rest of the past 14 ky (Fig. 2). By analogy with modern ETP dynamics, we suggest that the cooling is best explained by a shallower thermocline and a reduced influence of subtropical surface waters. This scenario is consistent with previous suggestions of a more La Niña–like state during the early to middle Holocene. Mg/Ca reconstructions from the equatorial Pacific indicate an enhanced zonal SST gradient at this time, with a colder eastern cold tongue and warmer western warm pool (Fig. 2) (*15*, *16*). At Baja California Sur, the cooling may have been amplified by a strengthened California Current (*17*). In contrast, alkenone-based SST reconstructions from both Baja California Sur (*18*) and the cold tongue (*19*) do not exhibit a mid-Holocene cooling. This disparity might be due to a summer/fall habitat for coccolithophores, resulting in an overprinting of La Niña–like cooling by orbitally forced seasonal radiative heating (*20*).

Numerical models of varying complexity have simulated a La Niña–like cooling of the ETP during the early to middle Holocene in response to enhanced boreal summer/fall insolation. Easterly winds strengthen because of zonally asymmetric heating of the tropical ocean and atmosphere (*21*, *22*), increased atmospheric baroclinicity (*23*), and/or intensification of the Asian summer monsoon (*24*). Although local Baja California Sur upwelling-favorable winds may also respond positively to orbital forcing, the maximum in spring insolation occurred much earlier (~15 ka) than our observed cooling. In support of more distant teleconnections, the shift toward warmer upwelling conditions just before 4 ka is close to the timing of widespread evidence for an abrupt and permanent weakening of the Asian summer monsoons (*25*), which may have helped the Pacific relax into a more El Niño–like state (*24*).

In addition to orbital-scale changes, the Soledad Basin Mg/Ca record displays strong variance at millennial time scales, as seen in the five-depth (nominally 200 to 300 years) running mean of the Mg/Ca data (Fig. 3). Before the data gap at ~5.9 to 6.5 ka, sample density is high enough (48 measurements per thousand years), and the relative noise low enough, to give us confidence that the smoothed record captures a meaningful millennial-scale climate history. We observe five cold intervals between ~7 and 11 ka, with roughly 1-ky spacing. In light of model- and proxy-based results supporting a solar influence on ENSO over the past millennium (*3*, *6*), we compare the smoothed record to cosmogenic nuclide proxies for solar activity.

For the period before the beginning of sunspot observations in A.D. 1610, reconstructions of solar variability are based on the cosmogenic nuclides ^{14}C (recorded in tree rings) (*26*) and ^{10}Be (preserved in polar ice cores) (*27*, *28*). An active Sun generates a higher total irradiance and a stronger interplanetary magnetic field that helps to shield Earth from the galactic cosmic rays that produce ^{14}C and ^{10}Be in the atmosphere. However, the relation between solar irradiance and cosmic-ray shielding is not well understood over long time scales. In addition, atmospheric levels of ^{14}C may be affected by changes in Earth's carbon cycle, ^{10}Be fluxes to ice sheets may be influenced by local climate, and the production rates of both nuclides are modulated by long-term variations in Earth's magnetic field. Nevertheless, the shared variance of high-pass–filtered (to correct for presumed slow variations in the geomagnetic field) ^{14}C and ^{10}Be records can be taken as an indication of fluctuations in solar activity over the Holocene.

Each of the early Holocene millennial-scale coolings at Soledad Basin corresponds to an inferred millennial-scale increase in solar activity (decreased cosmogenic nuclides) (Fig. 3). Cross-wavelet analysis of the unsmoothed data indicates significant common power (in phase) between Mg/Ca and the nuclides in the ~800- to 1000-year band (fig. S2). After performing a ~250-year smoothing and $\frac{1}{1800}$ $year^{-1}$ high-pass filtering of each record, Mg/Ca (before the ~5.9-6.5 ka data gap) correlates significantly with ^{14}C production ($r = 0.49$, $p = 0.02$, with 50-year lag on Mg/Ca) and reasonably well with ^{10}Be flux ($r = 0.41$, $p = 0.07$, with 100-year lag on Mg/Ca) (Fig. 4) (*13*). These correlations are based on completely independent age models. Given the strong link between this region and ENSO variability today, we suggest that this correspondence

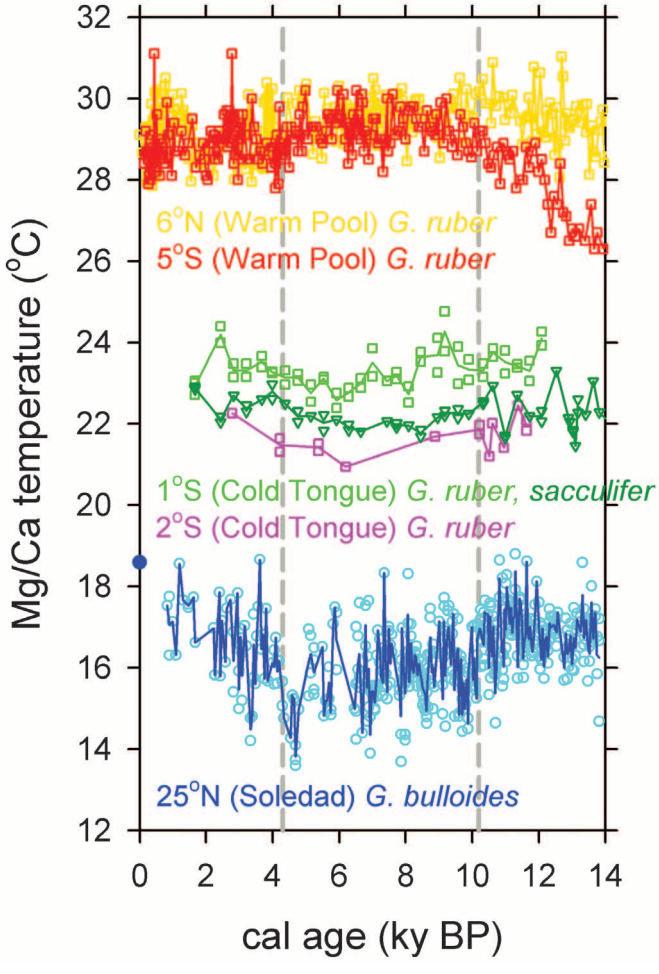

Fig. 2. SST reconstructions based on Mg/Ca in surface-dwelling planktonic foraminifera from the western equatorial Pacific warm pool (*15*) (gold and red), eastern equatorial Pacific cold tongue (*16*) (green and pink), and Soledad Basin (this study) (blue). Symbols denote individual measurements, and lines trace the mean at each depth. Along the equator, *G. ruber* and *G. sacculifer* are believed to represent mean annual conditions, whereas at Soledad Basin, *G. bulloides* reflects spring upwelling. The solid blue circle on the *y* axis denotes the modern average SST during the coldest month of the year (spring peak upwelling) at Soledad Basin (*9*). Vertical gray dashed lines bracket the early to middle Holocene interval of increased zonal SST gradient. BP, before the present.

provides support for the idea that the ocean dynamical thermostat (*4*) acts effectively at centennial-millennial time scales (*3*). Indeed, these early Holocene oscillations between warm El Niño–like and cool La Niña–like conditions were recently predicted by solar-forcing experiments using the Zebiak-Cane model (*29*). Although it is possible that local upwelling-favorable winds responded directly to positive solar forcing and amplified the cool SST signal, we argue, on the basis of modern observations (Fig. 1), that the impact would have been minor without a concomitant La Niña–like shoaling of the regional thermocline. Between ~2.2 and 5.9 ka, the poor correlation between Mg/Ca and the solar proxies may be due to the lower sample density (less than half that of the earlier interval) and/or the reduced amplitude of inferred solar variability, in line with the model prediction (*29*).

The observed sensitivity of the tropical Pacific to modest radiative forcing may have been achieved through positive feedback with other regions that also responded to solar variability. La Niña has historically been associated with stronger summer monsoons over Asia, as both are linked to strong easterlies over the tropical Pacific (*30*). Oxygen isotopes from speleothems in southern China (*31*) and Oman (*32*) indicate monsoon strengthening during early Holocene solar maxima, suggesting that an Asian teleconnection may have helped push the Pacific into a La Niña–like state during these intervals, or vice versa. Although the period of overlap is relatively short, the smoothed speleothem records bear strong resemblance to the Soledad Basin SST history (China: $r = 0.74$, $p = 0.01$; Oman: $r = 0.76$, $p = 0.003$) (Fig. 4). It is interesting to note that during the interval of greatest mismatch between Soledad Basin and the solar proxies, the cave records agree with our SST history: At 8.2 ka, the ETP was in an El Niño–like state and the monsoons were weak, despite the inferred secular increase in solar activity. This apparent anomaly may be attributed to the well-known "8.2-ka event," during which a large Laurentide meltwater discharge is believed to have cooled the North Atlantic and Eurasia, thereby weakening the Asian summer monsoons (*33*), which possibly fostered El Niño–like conditions in the ETP.

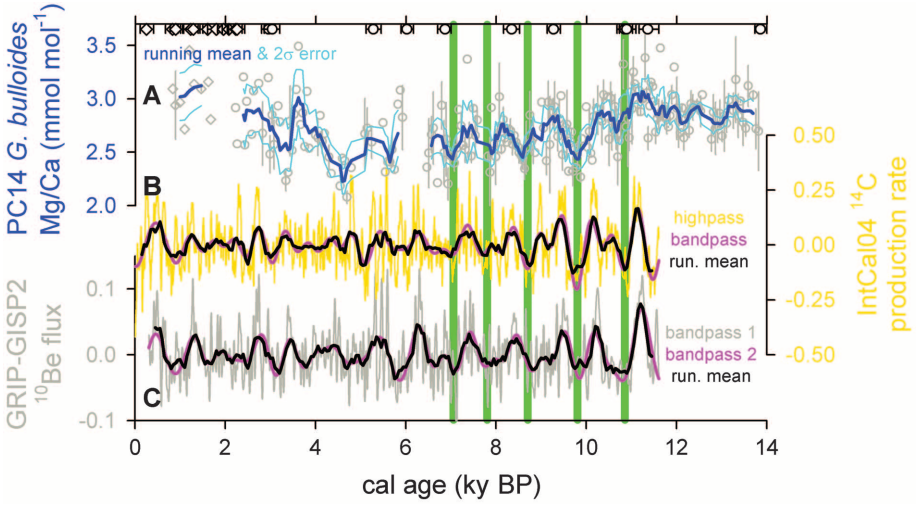

Fig. 3. Soledad Basin Mg/Ca record compared to solar proxies ^{14}C and ^{10}Be (*13*). (**A**) *G. bulloides* Mg/Ca mean and standard deviation at each depth (gray) with five-depth running mean (blue) and associated 2σ uncertainty estimate (light blue). Open black symbols at the top of the figure denote calibrated ^{14}C ages with 1σ errors. Diamonds are from GC41, and circles are from PC14. (**B**) Holocene tree-ring–derived $\Delta^{14}C$ (*26*) converted to ^{14}C production rate, with high values corresponding to low inferred solar activity. Data were high-pass filtered at $\frac{1}{1800}$ year^{-1} to remove secular changes that are probably related to Earth's magnetic field (gold), band-pass filtered at $\frac{1}{1800}$ to $\frac{1}{500}$ year^{-1} as in (*34*) (pink), and smoothed with a 250-year running mean before $\frac{1}{1800}$ year^{-1} high-pass filtering (black). (**C**) Holocene ice core ^{10}Be flux (*27*, *28*) filtered as in (B), except that the gray curve is a $\frac{1}{1800}$ to $\frac{1}{50}$ year^{-1} band pass that additionally eliminates subdecadal-scale noise. Green vertical lines indicate Soledad Basin cold intervals that correspond to times of increased solar activity.

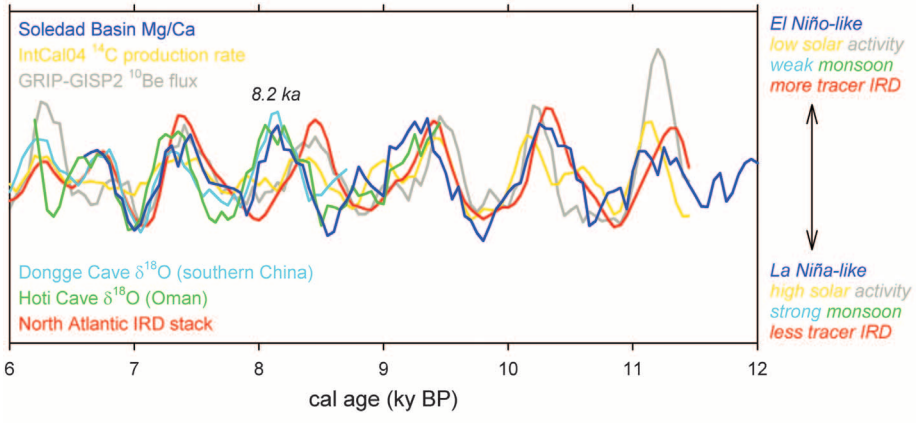

Fig. 4. Likely teleconnected climatic and solar proxy records spanning the early Holocene, each smoothed at ~250 years and high-pass filtered at $\frac{1}{1800}$ year^{-1} (*13*). Records are Soledad Basin *G. bulloides* Mg/Ca (this study) (blue), tree-ring–derived (*26*) ^{14}C production rate (gold), ice core ^{10}Be flux (*27*, *28*) (gray), Dongge Cave (southern China) stalagmite $\delta^{18}O$ (*31*) (light blue), Hoti Cave (Oman) stalagmite $\delta^{18}O$ (*32*) (green), and North Atlantic stack of IRD petrologic tracers (*34*) (red). All records are on their independent and untuned age models.

Additionally, Bond *et al.* (*34*) showed that there was increased ice-rafted debris (IRD) delivery from the Labrador and Nordic Seas into the North Atlantic during inferred Holocene solar minima. Their stacked IRD record correlates with Soledad Basin SSTs even more strongly than do the solar proxies ($r = 0.70$, $p < 0.001$, with 100-year lag on Mg/Ca) (Fig. 4). A cold North Atlantic during solar minima may have reinforced ETP warming through either the Asian monsoon linkage (*24*) or a southward shift of the intertropical convergence zone (*16*). Closure of this hypothetical positive feedback loop has been suggested to occur through an El Niño–forced shift in the prevailing winds that deliver drift ice from the Nordic Seas into the North Atlantic (*29*).

Persistent, decadal-scale droughts over the western United States have been linked to La Niña–like SST patterns in the ETP during the instrumental period (*35*). Tree-ring reconstructions extend this relationship back to the Medieval Warm Period (MWP, A.D. ~900 to 1300), which was seemingly characterized by positive solar forcing, inactive tropical volcanism, La Niña–like conditions, and multidecadal "megadroughts" (*3*, *5*, *6*, *35*). The first high-resolution, continuous Holocene speleothem proxy precipitation record from the southwestern United States documents a robust connection between inferred solar-activity maxima and dry conditions, which may be explained by solar forcing of La Niña–like states (*36*). Taken together with our SST record, these observations are consistent with solar-induced dynamical cooling of the ETP and provide predictions for millennial-scale fluctuations in the hydrologic balance over the western United States during the early Holocene.

GCMs fail to reproduce the La Niña–like nature of the MWP because the ocean thermostat mechanism is either absent or dampened by atmospheric effects in such models (*6*, *7*). If our observations are supported by future SST reconstructions from the equatorial Pacific, then it is possible that the sensitivity of the climate system to solar forcing is underestimated by current GCMs. The nature of the climate response appears to be one of

shifting atmosphere-ocean circulation patterns, with the tendency for global radiative surface warming being countered by the ocean dynamical thermostat.

References and Notes

1. J. L. Lean, *Geophys. Res. Lett.* **27**, 2425 (2000).
2. G. A. Meehl, J. M. Arblaster, K. Matthes, F. Sassi, H. van Loon, *Science* **325**, 1114 (2009).
3. M. E. Mann, M. A. Cane, S. E. Zebiak, A. Clement, *J. Clim.* **18**, 447 (2005).
4. A. C. Clement, R. Seager, M. A. Cane, S. E. Zebiak, *J. Clim.* **9**, 2190 (1996).
5. K. M. Cobb, C. D. Charles, H. Cheng, R. L. Edwards, *Nature* **424**, 271 (2003).
6. M. E. Mann *et al.*, *Science* **326**, 1256 (2009).
7. G. A. Vecchi, A. Clement, B. J. Soden, *Eos* **89**, 81 (2008).
8. A. van Geen *et al.*, *Paleoceanography* **18**, 1098 (2003).
9. R. W. Reynolds, N. A. Rayner, T. M. Smith, D. C. Stokes, W. Q. Wang, *J. Clim.* **15**, 1609 (2002).
10. F. B. Schwing, M. O'Farrell, J. M. Steger, K. Baltz, "Coastal Upwelling Indices West Coast of North America 1946-96," *NOAA Tech. Memo. NOAA-TM-NMFS-SWSFC-231* [National Oceanic and Atmospheric Administration (NOAA), Washington, DC, 1996].
11. F. B. Schwing, T. Murphree, L. deWitt, P. M. Green, *Prog. Oceanogr.* **54**, 459 (2002).
12. R. Durazo, T. R. Baumgartner, *Prog. Oceanogr.* **54**, 7 (2002).
13. Methods are available as supporting material on *Science* Online.
14. L. R. Sautter, R. C. Thunell, *Paleoceanography* **6**, 307 (1991).
15. L. Stott *et al.*, *Nature* **431**, 56 (2004).
16. A. Koutavas, P. B. deMenocal, G. C. Olive, J. Lynch-Stieglitz, *Geology* **34**, 993 (2006).
17. J. A. Barron, D. Bukry, *Palaeogeogr. Palaeoclimatol. Palaeoecol.* **248**, 313 (2007).
18. T. D. Herbert *et al.*, *Science* **293**, 71 (2001); 10.1126/science.1059209.
19. A. Koutavas, J. P. Sachs, *Paleoceanography* **23**, PA4205 (2008).
20. G. Leduc, R. Schneider, J. H. Kim, G. Lohmann, *Quat. Sci. Rev.* **29**, 989 (2010).
21. A. C. Clement, R. Seager, M. A. Cane, *Paleoceanography* **15**, 731 (2000).
22. B. L. Otto-Bliesner, E. C. Brady, S.-I. Shin, Z. Liu, C. Shields, *Geophys. Res. Lett.* **30**, 2198 (2003).
23. A. B. G. Bush, *Geophys. Res. Lett.* **26**, 99 (1999).
24. Z. Liu, J. Kutzbach, L. Wu, *Geophys. Res. Lett.* **27**, 2265 (2000).
25. C. Morrill, J. T. Overpeck, J. E. Cole, *Holocene* **13**, 465 (2003).
26. P. J. Reimer *et al.*, *Radiocarbon* **46**, 1029 (2004).
27. R. C. Finkel, K. Nishiizumi, *J. Geophys. Res. Oceans* **102**, 26699 (1997).
28. M. Vonmoos, J. Beer, R. Muscheler, *J. Geophys. Res. Space Phys.* **111**, A10105 (2006).
29. J. Emile-Geay, M. Cane, R. Seager, A. Kaplan, P. Almasi, *Paleoceanography* **22**, PA3210 (2007).
30. P. J. Webster *et al.*, *J. Geophys. Res.* **103**, 14451 (1998).
31. Y. J. Wang *et al.*, *Science* **308**, 854 (2005).
32. U. Neff *et al.*, *Nature* **411**, 290 (2001).
33. R. B. Alley *et al.*, *Geology* **25**, 483 (1997).
34. G. Bond *et al.*, *Science* **294**, 2130 (2001); 10.1126/science.1065680.
35. E. R. Cook, R. Seager, M. A. Cane, D. W. Stahle, *Earth Sci. Rev.* **81**, 93 (2007).
36. Y. Asmerom, V. Polyak, S. Burns, J. Rassmussen, *Geology* **35**, 1 (2007).

37. We thank P. Cappa, D. Lopez, D. Weller, and C. Wolak for laboratory assistance. This manuscript was improved by comments from B. Fox-Kemper and S. Lehman. This work was supported by collaborative NSF grants OCE-0214221 and OCE-0214646. R.M. is supported by the Royal Swedish Academy of Sciences through a grant financed by the Knut and Alice Wallenberg Foundation. Data are available at the NOAA National Climatic Data Center for Paleoclimatology.

Supporting Online Material

www.sciencemag.org/cgi/content/full/330/6009/1378/DC1
Methods
SOM Text
Figs. S1 to S3
Table S1
References

9 July 2010; accepted 29 October 2010
10.1126/science.1194887

Plasticity of Animal Genome Architecture Unmasked by Rapid Evolution of a Pelagic Tunicate

France Denoeud,[1,2,3] Simon Henriet,[4]* Sutada Mungpakdee,[4]* Jean-Marc Aury,[1,2,3]* Corinne Da Silva,[1,2,3]* Henner Brinkmann,[5] Jana Mikhaleva,[4] Lisbeth Charlotte Olsen,[4] Claire Jubin,[1,2,3] Cristian Cañestro,[6,24] Jean-Marie Bouquet,[4] Gemma Danks,[4,7] Julie Poulain,[1,2,3] Coen Campsteijn,[4] Marcin Adamski,[4] Ismael Cross,[8] Fekadu Yadetie,[4] Matthieu Muffato,[9] Alexandra Louis,[9] Stephen Butcher,[10] Georgia Tsagkogeorga,[11] Anke Konrad,[22] Sarabdeep Singh,[12] Marit Flo Jensen,[4] Evelyne Huynh Cong,[4] Helen Eikeseth-Otteraa,[4] Benjamin Noel,[1,2,3] Véronique Anthouard,[1,2,3] Betina M. Porcel,[1,2,3] Rym Kachouri-Lafond,[13] Atsuo Nishino,[14] Matteo Ugolini,[4] Pascal Chourrout,[15] Hiroki Nishida,[14] Rein Aasland,[16] Snehalata Huzurbazar,[12] Eric Westhof,[13] Frédéric Delsuc,[11] Hans Lehrach,[17] Richard Reinhardt,[17] Jean Weissenbach,[1,2,3] Scott W. Roy,[18] François Artiguenave,[1,2,3] John H. Postlethwait,[6] J. Robert Manak,[10] Eric M. Thompson,[4,19] Olivier Jaillon,[1,2,3] Louis Du Pasquier,[20] Pierre Boudinot,[21] David A. Liberles,[22] Jean-Nicolas Volff,[23] Hervé Philippe,[5] Boris Lenhard,[4,7,19] Hugues Roest Crollius,[9] Patrick Wincker,[1,2,3]† Daniel Chourrout[4]†

Genomes of animals as different as sponges and humans show conservation of global architecture. Here we show that multiple genomic features including transposon diversity, developmental gene repertoire, physical gene order, and intron-exon organization are shattered in the tunicate *Oikopleura*, belonging to the sister group of vertebrates and retaining chordate morphology. Ancestral architecture of animal genomes can be deeply modified and may therefore be largely nonadaptive. This rapidly evolving animal lineage thus offers unique perspectives on the level of genome plasticity. It also illuminates issues as fundamental as the mechanisms of intron gain.

Tunicates, viewed as the closest living relatives of vertebrates, were probably simplified from more complex chordate ancestors (*1*). Larvacean tunicates represent the second most abundant component of marine zooplankton and filter small particles by their gelatinous house. *Oikopleura dioica* is the most cosmopolitan larvacean, has a very short life cycle (4 days at 20°C), and can be reared in the laboratory for hundreds of generations (*2*). Unique among tunicates, it has separate sexes. We sequenced its genome with high-coverage shotgun reads (14X) using males resulting from 11 successive full-sib matings (figs. S1 and S2 and tables S1 to S3) (*3*). Two distinct haplotypes were retained, despite inbreeding. Their comparison yielded a high estimate of population mutation rate ($\theta = 4N_e\mu = 0.0220$) that is consistent with a large effective population size (N_e) and/or a high mutation rate per generation (μ) (*3*). Sequence comparisons among populations from the eastern Pacific and eastern Atlantic and within the latter revealed low dN/dS values (dN, rate of substitutions at nonsilent sites; dS, rate of substitutions at silent sites) consistent with strong purifying selection, as expected for large populations (*3*). In 17 of 18

[1]Commissariat à l'Énergie Atomique, Institut de Génomique, Genoscope, Evry, France. [2]CNRS, UMR 8030, Evry, France. [3]Université d'Evry, Evry, France. [4]Sars International Centre for Marine Molecular Biology, University of Bergen, Bergen, Norway. [5]Département de Biochimie, Université de Montréal, Montréal, Canada. [6]Institute of Neuroscience, University of Oregon, Eugene, OR 97403, USA. [7]Bergen Center for Computational Science, University of Bergen, Bergen, Norway. [8]Laboratorio de Genética, Universidad de Cádiz, Cádiz, Spain. [9]Dyogen Lab, Institut de Biologie de l'ENS (IBENS), CNRS-UMR8197, Ecole Normale Supérieure, Paris, France. [10]Department of Biology, University of Iowa, Iowa City, IA 52242–1324, USA. [11]Laboratoire de Paléontologie, Phylogénie et Paléobiologie, Institut des Sciences de l'Evolution, UMR 5554–CNRS, Université Montpellier II, Montpellier, France. [12]Department of Statistics, University of Wyoming, Laramie, WY 82071, USA. [13]Institut de Biologie Cellulaire et Moléculaire du CNRS, Université de Strasbourg, Strasbourg, France. [14]Department of Biological Sciences, Osaka University, Osaka, Japan. [15]Centre Hospitalier d'Albi, Albi, France. [16]Department of Molecular Biology, University of Bergen, Bergen, Norway. [17]Vertebrate Genomics, Max Planck Institute for Molecular Genetics, Berlin, Germany. [18]National Center for Biotechnology Information, National Library of Medicine, National Institutes of Health, Bethesda, MD 20894, USA. [19]Department of Biology, University of Bergen, Bergen, Norway. [20]Institute of Zoology and Evolutionary Biology, University of Basel, Basel, Switzerland. [21]Institut National de la Recherche Agronomique (INRA), Virologie et Immunologie Moléculaires, Jouy-en-Josas, France. [22]Department of Molecular Biology, University of Wyoming, Laramie, WY 82071, USA. [23]Institut de Génomique Fonctionnelle de Lyon, UMR 5242–CNRS/INRA/Université Claude Bernard Lyon 1/Ecole Normale Supérieure, Ecole Normale Supérieure de Lyon, Lyon, France. [24]Departament de Genètica, Universitat de Barcelona, Spain.

*These authors contributed equally to this work.
†To whom correspondence should be addressed. E-mail: Daniel.Chourrout@sars.uib.no (D.C.); pwincker@genoscope.cns.fr (P.W.)

Supporting Online Material for

Dynamical Response of the Tropical Pacific Ocean to Solar Forcing During the Early Holocene

Thomas M. Marchitto,* Raimund Muscheler, Joseph D. Ortiz, Jose D. Carriquiry, Alexander van Geen

*To whom correspondence should be addressed. E-mail: tom.marchitto@colorado.edu

Published 3 December 2010, *Science* **330**, 1378 (2010)
DOI: 10.1126/science.1194887

This PDF file includes:

Supporting Online Material

Modern hydrographic data

Local SSTs are from NOAA's National Centers for Environmental Prediction (NCEP) weekly 1° grid optimum interpolation analysis (version 2) using in situ and satellite SSTs (*1*). The Niño3 index is calculated from the same SST database. Both data sets are available at http://iridl.ldeo.columbia.edu/SOURCES. We note that the Soledad Basin correlation to ENSO (r = 0.61) is considerably stronger than to the related Pacific Decadal Oscillation (PDO) index (r = 0.36) (*2*). The upwelling index (offshore Ekman transport) is calculated by NOAA's Pacific Fisheries Environmental Laboratory (PFEL) using atmospheric pressure fields prepared by the U.S. Navy Fleet Numerical Meteorological and Oceanographic Center (FNMOC) (*3*). Data are available at the PFEL website (http://www.pfeg.noaa.gov/).

Age model

Twenty three foraminiferal samples were radiocarbon dated by accelerator mass spectrometry (AMS): 11 from GC41 (10 planktonic and 1 benthic) and 12 from PC14 (10 planktonic and 2 benthic) (Table S1). Three of the GC41 dates and all of the PC14 dates were previously published *(4)*. The published dates were on mixed planktonics (mostly the surface dwelling species *G. bulloides* and *G. ruber*) and mixed benthics (mostly *Bolivina* spp.), while the new dates were on monospecific *G. bulloides*. All dates were recalibrated using the online program Calib 6.0html (*5*) and the Marine09 calibration curve (*6*). We used reservoir age corrections (ΔR) of 200 ±100 yr for the planktonic ages (*4*) and 400 ±100 yr for the benthic ages. Age models were fit through the median calibrated ages from each core, using a straight line in GC41 and a 4^{th}-order polynomial in PC14 (Fig. S1A). Based on our previous work documenting the incursion of radiocarbon-depleted waters during Heinrich Stadial 1 and the Younger Dryas (*7*), we omit one date that falls within the interval that corresponds to the Younger Dryas according to our diffuse spectral reflectance (DSR) stratigraphy (Fig. S1B). After then placing the core on the resulting radiocarbon age model, the DSR change that signals the end of the Younger Dryas matches the Greenland ice core (GISP2) age of this event (*8*) within 50 yr (Fig S1).

Mg/Ca methods

Samples consisting of typically ~30-60 specimens of *G. bulloides* (250-355 μm) were crushed between glass microscope slides, with larger samples being split into two aliquots for replicate measurements. Crushed samples were cleaned reductively (using anhydrous hydrazine) and oxidatively (using H_2O_2) in a Class-1000 clean lab (*9, 10*). Multiple minor and trace elements were measured by magnetic-sector single-collector ICP-MS, on a Thermo-Finnigan Element2 (*11, 12*). Long-term 1σ precision for Mg/Ca, based on analysis of consistency standard solutions, is 0.5% across a wide range of Mg/Ca values and sample sizes.

Of 442 Mg/Ca measurements that met the minimum size cutoff of >5 μg $CaCO_3$, 5 were discarded because they yielded a standard deviation with their replicates that was >0.5 mmol mol^{-1}. The pooled standard deviation of the remaining replicates was 0.18 mmol mol^{-1} (dof = 213). Many of these replicates were based on separate samplings of the same interval, which leads to greater scatter than split aliquots of a crushed sample. An additional 4 unreplicated measurements were discarded because their standard deviation with one or both of their neighboring means was >0.7 mmol mol^{-1}. The total rejection rate was therefore 2.0% (9/442). Amongst all 442 samples, Mn/Ca was never >15 μmol mol^{-1}, indicating negligible carbonate

overgrowths. Fe/Ca was >200 μmol mol^{-1} in 6 samples and Al/Ca was >200 μmol mol^{-1} in 5 samples, but their Mg/Ca data were not excluded because they were not outliers. The >500-yr data gaps near 2 and 6 ka are due to relatively low abundances of *G. bulloides*.

Mg/Ca was converted to SST using a calibration based on laboratory-grown *G. bulloides* combined with core top samples (*13*), which has been verified using sediment trap samples from Santa Barbara Basin off of southern California (*14*). The standard error of this equation is quoted at ±0.8°C (*13*).

Cross wavelet analysis

To identify common spectral power and its phase relationship between the unsmoothed Mg/Ca data and the cosmogenic nuclide proxies, we computed cross wavelet transforms (*15*) (Fig. S2). Only the very high resolution portion of the Mg/Ca record was used (>6.5 ka, prior to the data gap). Data were first interpolated to 50 yr spacing (based on the nominal spacing of the Mg/Ca series) and linearly detrended. Strongest common power is at periods of ~800-1000 yr, significant at the 95% confidence level. Significant common power extends forward to ~8.5 ka versus ^{14}C production and to ~9.5 ka versus ^{10}Be flux. Phase angle within these regions ranges from 0° to a slight lag on Mg/Ca. At ~8-8.5 ka the common power diminishes and the lag grows, especially for ^{10}Be (~90°), probably because of the '8.2 ka event' as noted in the main text. The phase relationship with ^{10}Be is different from that with ^{14}C because the age models of the two cosmogenic time series differ (see Fig. 3). The tree-ring based chronology for ^{14}C (*16*) is believed to be more precise and accurate than the ice core chronology for ^{10}Be (*17*).

Data processing for comparing multi-centennial/millennial signals

Data processing to further examine the proposed relationship between solar forcing and the various proxy time series was motivated by two necessities. First, we wished to smooth the Mg/Ca series to eliminate high-frequency variability. This variability likely represents a combination of real climate fluctuations that are at too high a frequency to reliably correlate to other records (due to aliasing and age uncertainties), plus some proxy-related noise. We chose a 5-depth running mean, which equates to roughly 200-300 yr. We decided to smooth rather than lowpass filter so that the smoothed record would be based on actual measurements (since filtering requires interpolation first). The other records were smoothed at ~250 yr to match the Mg/Ca treatment as closely as possible. Second, we wished to remove long-term drift from the nuclide records that is likely related to slow variations in the geomagnetic field (*18*). We detrended and FFT highpass filtered each record at 1/1800 yr, following Bond et al. (*19, 20*). Although the best frequency cutoff is not known, the results are not very sensitive to this choice (Fig. S3). The proxy records were filtered in the same way to remove drift that is unlikely to be driven by solar variability. We aimed to be as consistent as possible in processing each record, but differences in sample spacing necessitated slightly different approaches.

Soledad Basin Mg/Ca: We calculated the running mean of individual values from 5 consecutive depths in the core (Fig. 3A), followed by 50-yr interpolation, linear detrend, and 1/1800 yr highpass filter (Fig. 4).

^{14}C production rate: Production rate after the end of the Younger Dryas was first calculated from IntCal04 $\Delta^{14}C$ data (*16*) using a box-diffusion model with the carbon cycle held constant (*21-23*). We then calculated the 251-yr running mean of annual production rate data, followed by linear detrend, 1/1800 yr highpass filter, and 50-yr resampling (Fig. 3B, 4).

^{10}Be flux: Flux after the end of the Younger Dryas was first calculated from GISP2 (*24*) and GRIP (*25*) ^{10}Be records, which combined provide a continuous Holocene record. Records were combined after correcting for differences between average ^{10}Be concentrations for periods of overlap and after correcting for timescale differences between the GRIP and GISP2 chronologies. Flux data is reported on the GICC05 timescale (*17*), which was also used to derive accumulation rates for the flux calculations. Thinning of layers due to ice flow was corrected for using the strain rate from the ss09sea model (*26*). We then calculated the 249-yr running mean of interpolated biennial flux data, followed by linear detrend, 1/1800 yr highpass filter, and 50-yr resampling (Fig. 3C, 4).
Dongge Cave $\delta^{18}O$: Using data on untuned U-Th age model (*27*). We performed a 5-yr interpolation, followed by 250-yr running mean, linear detrend, 1/1800 yr highpass filter, and 50-yr resampling (Fig. 4).
Hoti Cave $\delta^{18}O$: Using data on untuned U-Th age model (*28*). We performed a 5-yr interpolation, followed by 250-yr running mean, linear detrend, 1/1800 yr highpass filter, and 50-yr resampling (Fig. 4).
Bond IRD stack: Using 70-yr interpolated stack data on untuned calibrated ^{14}C age model (*19*). We calculated the 3-point running mean, followed by 50-yr interpolation, linear detrend, and 1/1800 yr highpass filter (Fig. 4).

Fig. 3 shows that for the nuclide records, both the approach described above (black) and the 1/1800-1/500 yr bandpass approach of Bond et al. (*19, 20*) (pink) capture the multi-centennial to millennial scale variability inherent in the original data.

The running 2σ error envelope on Mg/Ca shown in Fig. 3A is based on the standard error of mean values from 5 consecutive depths, where n is the total number of individual measurements in that interval. Correlation coefficients were calculated at various time lags. We report the maximum correlation found within several 50-yr time steps. The greatest lag found was 100 yr, which is well within the combined age uncertainty of the various time series comparisons. Therefore we do not consider the lag magnitudes themselves to be meaningful. P-values were calculated using the reduced degrees of freedom that resulted from smoothing the Mg/Ca record (dof = (n-2)/5, where n is the number of time steps that the correlation is calculated over).

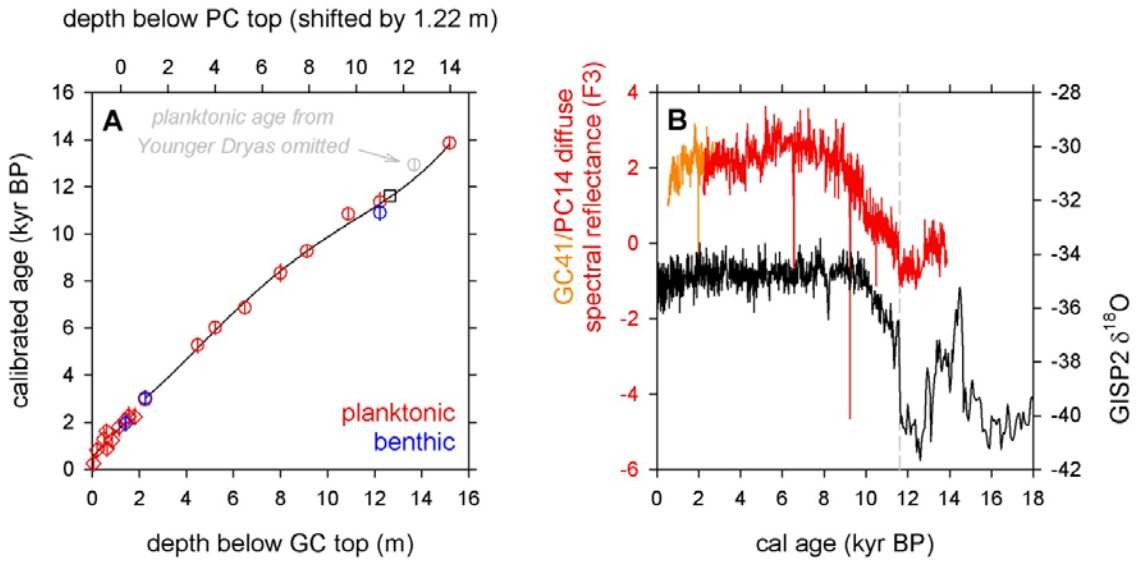

Fig. S1. (**A**) Polynomial age models (black lines) fit through calibrated radiocarbon ages from GC41 (diamonds) and PC14 (circles). Symbols are median ages with 2σ error ranges. Gray date was omitted from the fit (see text). Black square denotes the age of the end of the Younger Dryas in Greenland ice core GISP2 (*8*) and the depth of this event in PC14 as inferred from the DSR record shown in panel (**B**). This point was not used in generating the polynomial age model. The depth scales for the two cores are offset according to (*4*) but this detail has no effect on the age models. (**B**) GC41/PC14 DSR factor 3, which exhibits a strong correlation to productivity proxies along this margin (*7, 29*), plotted on the age models from panel (**A**) and compared to GISP2 $\delta^{18}O$ (*8*). Previous work has shown that DSR stratigraphies from this region closely mimic Greenland $\delta^{18}O$, with abrupt transitions likely being synchronous (*7, 29*). Gray dashed line denotes the GISP2 age of the end of the Younger Dryas (11.61 ka).

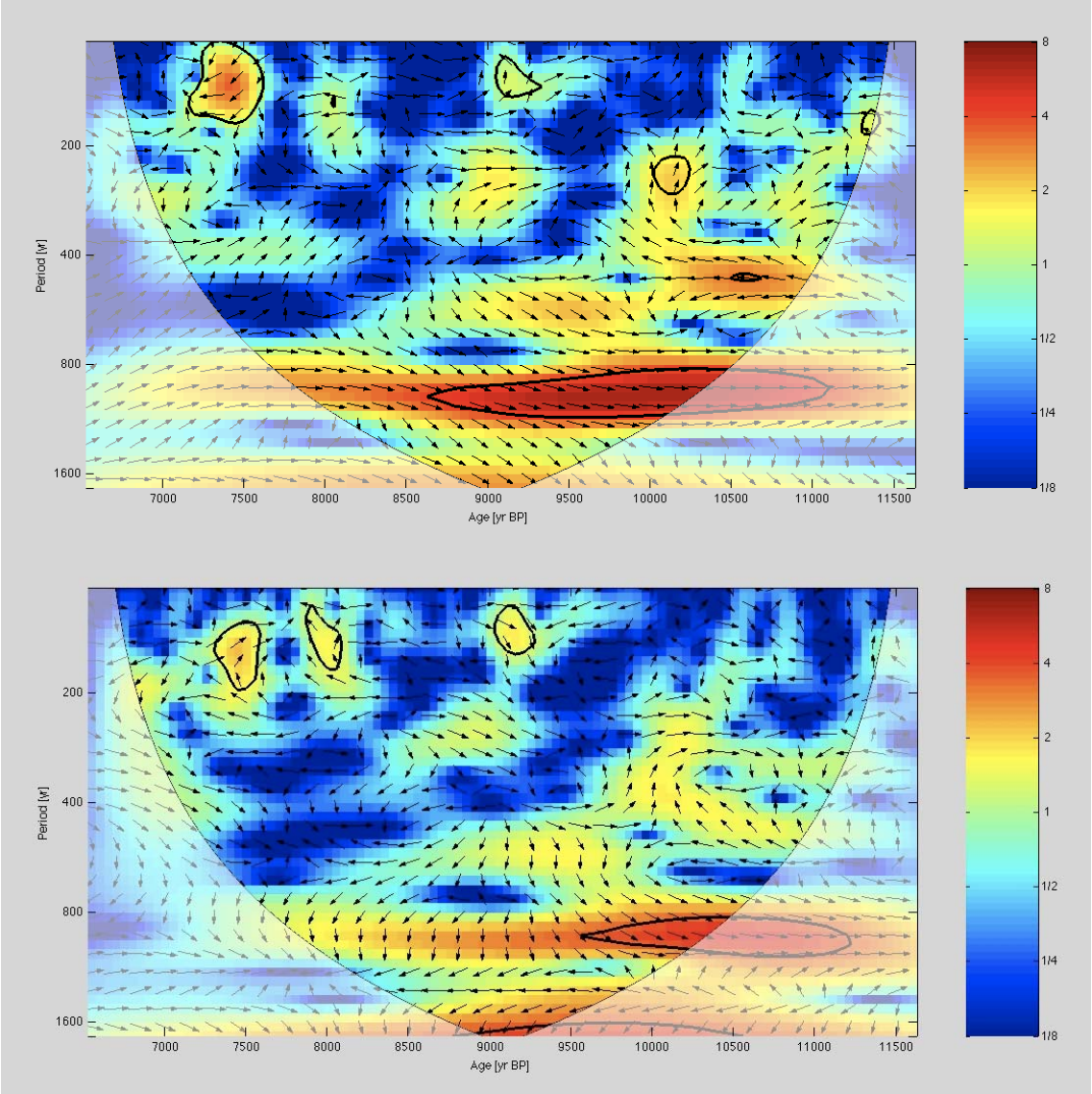

Fig. S2. Cross wavelet transforms (*15*) of Soledad Basin Mg/Ca vs. (top) cosmogenic ^{14}C production and (bottom) ^{10}Be flux. Warm colors indicate regions of high common spectral power between the two time series. Regions within bold black contours are significant at the 95% confidence level against red noise. Small areas of significant common power at short periods (~100-300 yr) are not meaningful because of age model uncertainties. Arrows denote phase angle, with in-phase pointing right, anti-phase pointing left, and 90° lag on Mg/Ca pointing down. Clouded region denotes the Cone of Influence where edge effects cannot be ignored.

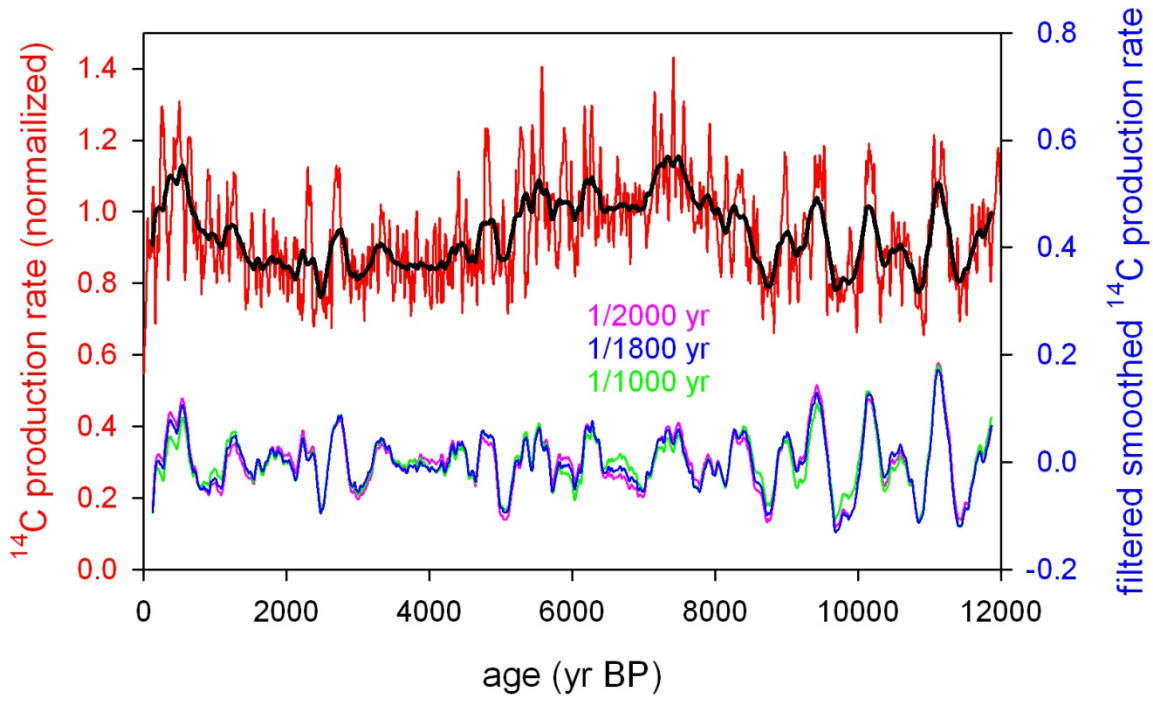

Fig. S3. Comparison of three choices for the highpass filtering of the smoothed ^{14}C production record. Shown are the normalized raw production data (red) and 251-yr running mean (black); and highpass filtered versions of the 251-yr running mean using cutoffs of 1/2000 yr (pink), 1/1800 yr (*19, 20*) (blue), and 1/1000 yr (green).

Table S1. Radiocarbon ages and calibrated ages (Calib 6.0html) for Soledad Basin core MV99-GC41/PC14.

Core	Depth	Taxa[a]	^{14}C age	age error	Reference	Accession #	Cal age[b]	1s cal range[c]	2s cal range[c]
GC41	5.5	*G. bulloides*	815	110	this study	OS-58938	250	109-406	0-471
GC41	20.5	*G. bulloides*	1470	110	this study	OS-58934	826	670-947	553-1124
GC41	50.5	*G. bulloides*	1930	170	this study	OS-58943	1286	1072-1495	881-1729
GC41	60.5	*G. bulloides*	2230	95	this study	OS-58936	1603	1434-1759	1297-1904
GC41	64	mixed planktonics	1550	35	(*1*)		894	770-1000	679-1122
GC41	85.5	*G. bulloides*	1880	130	this study	OS-58941	1229	1048-1392	896-1587
GC41	115.5	*G. bulloides*	2400	120	this study	OS-58940	1798	1603-1980	1406-2168
GC41	142	mixed planktonics	2630	45	(*1*)		2075	1930-2210	1818-2326
GC41	142	mixed benthics	2730	35	(*1*)		1955	1825-2087	1700-2245
GC41	155.5	*G. bulloides*	2780	90	this study	OS-59232	2256	2068-2428	1937-2653
GC41	181.5	*G. bulloides*	2760	75	this study	OS-59235	2228	2042-2363	1917-2599
PC14	103	mixed planktonics	3350	35	(*1*)		2955	2799-3074	2726-3226
PC14	103	mixed benthics	3610	95	(*1*)		3031	2853-3199	2730-3352
PC14	326	mixed planktonics	5150	65	(*1*)		5272	5114-5444	4951-5565
PC14	401	mixed planktonics	5810	70	(*1*)		6013	5892-6164	5731-6269
PC14	526	mixed planktonics	6580	70	(*1*)		6860	6699-7003	6568-7157
PC14	678	mixed planktonics	8070	130	(*1*)		8337	8161-8512	7967-8721
PC14	790	mixed planktonics	8820	75	(*1*)		9265	9126-9420	8982-9515
PC14	966	mixed planktonics	10100	50	(*1*)		10840	10672-11020	10569-11122
PC14	1101	mixed planktonics	10500	55	(*1*)		11356	11167-11602	11103-11755
PC14	1101	mixed benthics	10350	85	(*1*)		10888	10729-11092	10577-11172
PC14	1246	mixed planktonics	11650	80	(*1*)		12929	12787-13089	12650-13182
PC14	1396	mixed planktonics	12600	65	(*1*)		13853	13732-13994	13572-14141

[a] Depths are given in cm below top of GC or PC.
[b] $\Delta R = 200 \pm 100$ yr for planktonics and 400 ± 100 yr for benthics.
[c] Cal age ranges with <2% probability are not listed

References

1. R. W. Reynolds, N. A. Rayner, T. M. Smith, D. C. Stokes, W. Q. Wang, *Journal of Climate* **15**, 1609 (2002).
2. N. J. Mantua, S. R. Hare, Y. Zhang, J. M. Wallace, R. C. Francis, *Bulletin of the American Meteorological Society* **78**, 1069 (1997).
3. F. B. Schwing, M. O'Farrell, J. Steger, K. Baltz, *NOAA Tech. Memo.* **NOAA-TM-NMFS-SWFC-231**, 207 pp. (1996).
4. A. van Geen *et al.*, *Paleoceanography* **18**, doi:10.1029/2003PA000911 (2003).
5. M. Stuiver, P. J. Reimer, *Radiocarbon* **35**, 215 (1993).
6. P. J. Reimer *et al.*, *Radiocarbon* **51**, 1111 (2009).
7. T. M. Marchitto, S. J. Lehman, J. D. Ortiz, J. Flückiger, A. van Geen, *Science* **316**, 1456 (2007).
8. P. M. Grootes, M. Stuiver, *Journal of Geophysical Research* **102**, 26455 (1997).
9. E. A. Boyle, L. D. Keigwin, *Earth and Planetary Science Letters* **76**, 135 (1985).
10. E. A. Boyle, Y. Rosenthal, in *The South Atlantic: Present and Past Circulation,* G. Wefer, e. al., Eds. (Springer-Verlag, Berlin, 1996), pp. 423-443.
11. Y. Rosenthal, M. P. Field, R. M. Sherrell, *Analytical Chemistry* **71**, 3248 (1999).
12. T. M. Marchitto, *Geochemistry, Geophysics, Geosystems* **7**, Q05P13 (2006).
13. T. A. Mashiotta, D. W. Lea, H. J. Spero, *Earth and Planetary Science Letters* **170**, 417 (1999).
14. D. K. Pak, D. W. Lea, J. P. Kennett, *Geochem. Geophys. Geosyst.* **5**, (2004).
15. A. Grinsted, J. C. Moore, S. Jevrejeva, *Nonlinear Processes in Geophysics* **11**, 561 (2004).
16. P. J. Reimer, et al., *Radiocarbon* **46**, 1029 (2004).
17. B. M. Vinther *et al.*, *Journal of Geophysical Research-Atmospheres* **111**, (2006).
18. G. Wagner *et al.*, *Nuclear Instruments and Methods in Physics Research Section B: Beam Interactions with Materials and Atoms* **172**, 597 (2000).
19. G. Bond *et al.*, *Science* **294**, 2130 (2001).
20. R. Muscheler, J. Beer, B. Kromer, in *International Solar Cycle Studies Symposium (ISCS 2003)*. (Tatranska Lomnic, Slovakia, 2003), vol. 535, pp. 305-316.
21. U. Siegenthaler, *J. Geophys. Res.* **88**, 3599 (1983).
22. M. Stuiver, P. D. Quay, *Science* **207**, 11 (1980).
23. R. Muscheler, R. Beer, P. W. Kubik, H. A. Synal, *Quaternary Science Reviews* **24**, 1849 (2005).
24. R. C. Finkel, K. Nishiizumi, *J. Geophys. Res.-Oceans* **102**, 26699 (1997).
25. M. Vonmoos, J. Beer, R. Muscheler, *Journal of Geophysical Research-Space Physics* **111**, (2006).
26. S. J. Johnsen *et al.*, *J. Quat. Sci.* **16**, 299 (2001).
27. Y. J. Wang *et al.*, *Science* **308**, 854 (2005).
28. U. Neff *et al.*, *Nature* **411**, 290 (2001).
29. J. D. Ortiz *et al.*, *Geology* **32**, 521 (2004).